

Deep learning of experimental electrochemistry for battery cathodes across diverse compositions

Peichen Zhong,^{1,2,*} Bowen Deng,^{1,2} Tanjin He,^{1,2} Zhengyan Lun,^{1,3} and Gerbrand Ceder^{1,2,†}

¹*Department of Materials Science and Engineering,
University of California, Berkeley, California 94720, United States*

²*Materials Sciences Division, Lawrence Berkeley National Laboratory, California 94720, United States*

³*School of Chemical Sciences, University of Chinese Academy of Sciences, Beijing 100049, China*

(Dated: April 12, 2023)

Artificial intelligence (AI) has emerged as a powerful tool in the discovery and optimization of novel battery materials. However, the adoption of AI in battery cathode representation and discovery is still limited due to the complexity of optimizing multiple performance properties and the scarcity of high-fidelity data. In this study, we present a comprehensive machine-learning model (DRXNet) for battery informatics and demonstrate the application in discovery and optimization of disordered rocksalt (DRX) cathode materials. We have compiled the electrochemistry data of DRX cathodes over the past five years, resulting in a dataset of more than 30,000 discharge voltage profiles with 14 different metal species. Learning from this extensive dataset, our DRXNet model can automatically capture critical features in the cycling curves of DRX cathodes under various conditions. Illustratively, the model gives rational predictions of the discharge capacity for diverse compositions in the Li–Mn–O–F chemical space and high-entropy systems. As a universal model trained on diverse chemistries, our approach offers a data-driven solution to facilitate the rapid identification of novel cathode materials, accelerating the development of next-generation batteries for carbon neutralization.

I. INTRODUCTION

The pursuit of carbon neutrality has become a global imperative in the face of climate change, driving the transition to renewable energy sources and the widespread adoption of electric vehicles [1–3]. High-performance battery cathode materials with large energy density, high-rate performance, and long cycle life are central to these advancements. The development of new cathode materials is essential to meeting the increasing demand for energy storage and advancing the electrification of transportation systems [4].

Artificial intelligence (AI) has emerged as a powerful tool in the discovery and optimization of novel battery materials [5]. By leveraging vast amounts of experimental and computational data, AI-assisted techniques can accelerate the battery design process by identifying promising candidates within large chemical spaces [6], uncovering hidden structure–property relationships via machine-learned atomistic modeling [7], predicting battery remaining lifespan [8–10], and optimizing the fast charge/discharge protocol [11]. These efforts significantly reduce the time and cost required for conventional trial-and-error approaches. Most recently, the battery data genome initiative has been proposed to use AI assistance to accelerate the discovery and optimization of battery materials [12].

Despite these advancements, current machine-learning efforts in battery research primarily focus on predicting the lifespan within one battery system in a rather simple

chemical space, such as NMC (Ni–Mn–Co). The development of exploratory machine learning for representing chemical effects in a more complicated multi-dimensional chemical space remains underdeveloped due to the challenges associated with simultaneously optimizing multiple electrochemical properties (e.g., rate capability, cyclability, and various test voltage windows) and capturing the complex chemistry among different transition metal (TM) species [13]. Moreover, the scarcity of high-fidelity data further hinders the progress of AI in the battery field.

Specifically, disordered rocksalt (DRX) materials emerge as promising cathode materials that make use of earth-abundant precursors and can enable scaling of Li-ion energy storage to several TWh/year production [14]. Owing to the nearly unlimited compositional design space and considerably more complex structure–property relationship of DRX cathodes compared with conventional layered cathodes (Fig. 1A), their rational design requires the extensive involvement of advanced characterization techniques (e.g., pair-distribution function analysis [15], spherical-aberration-corrected transmission electron microscopy [16], solid-state nuclear magnetic resonance spectroscopy [17]) as well as complicated computational tools (e.g., high-dimensional cluster expansion and Monte Carlo simulation [18, 19]) under a conventional frame of investigation. Data-driven methods offer alternative means of compositional design and optimization of high-dimensional DRX cathodes without having to fully construct their structure–property relationships.

In light of these challenges, we developed DRXNet, an exploratory machine-learning model for the discovery and optimization of battery cathode materials. DRXNet uses composition, test current density, working voltage

* zhongpc@berkeley.edu

† gceder@berkeley.edu

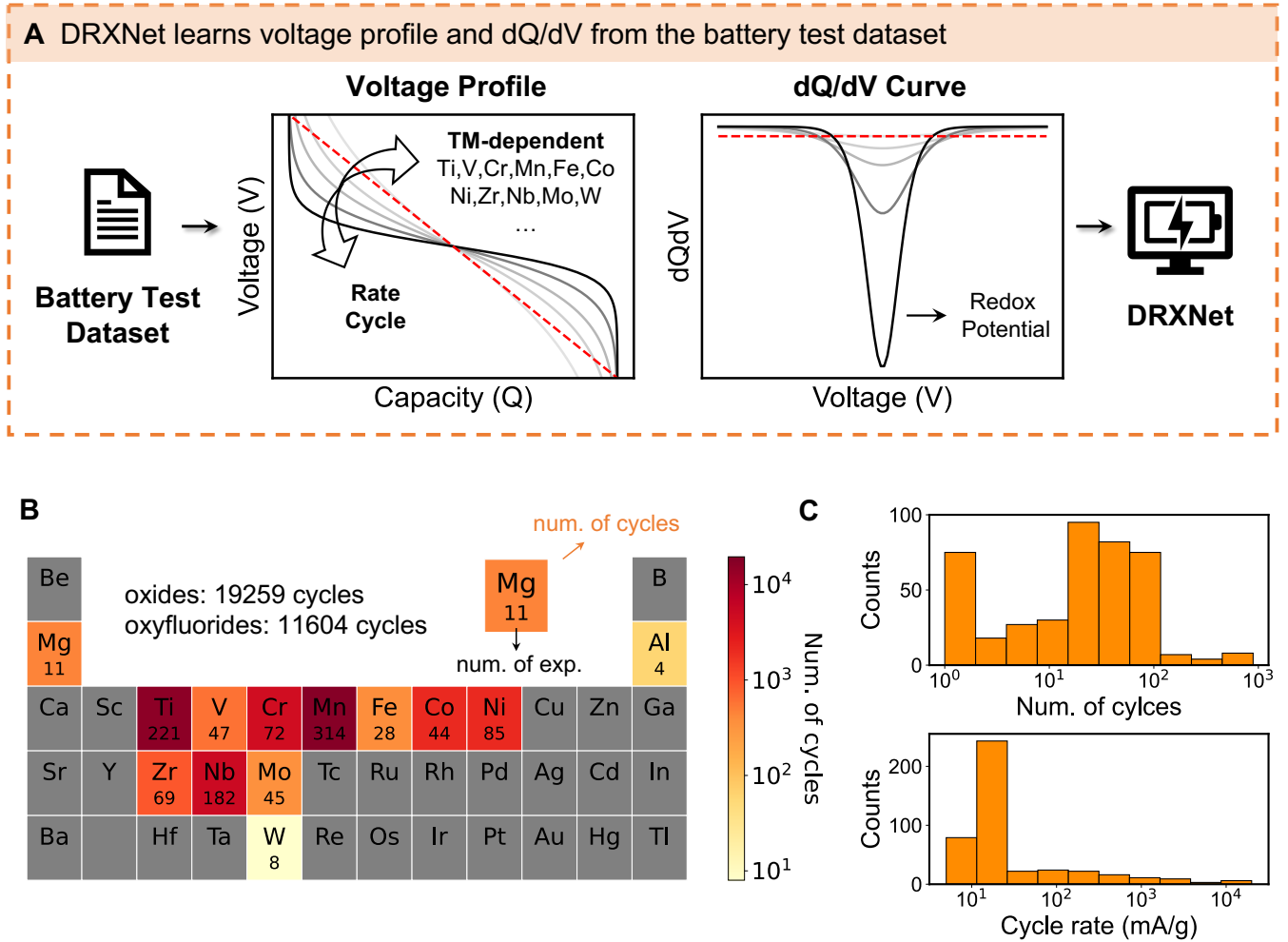


FIG. 1. **Introduction to discharge voltage profiles and the collected experimental DRX-TD dataset.** (A) The voltage profile illustrates the relationship between capacity (Q) and voltage (V). The derivative quantity dQ/dV peaks at the redox potential of the TM, where a pronounced peak indicates a flat plateau in the voltage profile. (B) The elemental distribution of collected experimental electrochemistry data. In total, the dataset contains 19,259 discharge profiles collected from DRX oxides and 11,604 discharge profiles from oxyfluorides. The color-coded boxes indicate the number of discharge profiles (cycles) on compounds that contain that specific element. The number within each elemental box represents the count of individual experiments conducted. (C) A histogram of the number of cycles (N_{cycle}) and current density (rate) for all the individual electrochemical tests.

window, and cycle number as inputs to predict entire discharge voltage profiles. By training and testing on over 30,000 experimental discharge voltage profiles of DRX materials comprising various metal species, we show that the model accurately captures the cathode electrochemistry under different test conditions. Notably, DRXNet captures cycled discharge capacity in diverse Li-Mn-O-F compositions and makes rational predictions for several high-entropy systems. As a universal model trained on diverse chemistries, DRXNet offers a data-driven solution to facilitate the rapid identification of novel cathode materials with improved energy-storage capabilities and paves the way for the development of next-generation batteries that can power a carbon-neutral future.

II. RESULTS

A. DRX Battery Test Dataset

A prototype binary DRX cathode ($\text{Li}_{1+x}\text{M}'_a\text{M}''_b\text{O}_{2-y}\text{F}_y$) is composed of three primary compositional parameters: (1) the redox-active species M' ; (2) the inert high-valent TM M'' , which compensates for the Li excess and stabilizes disordered structures [22]; (3) fluorine, which enhances the cyclability and accommodates more Li excess without losing TM redox by reducing the anion valence [23]. As shown in Fig. 1A, the discharge-voltage profile presents a negative slope of voltage against capacity. This profile shape is tied to various factors such as the DRX composition, applied

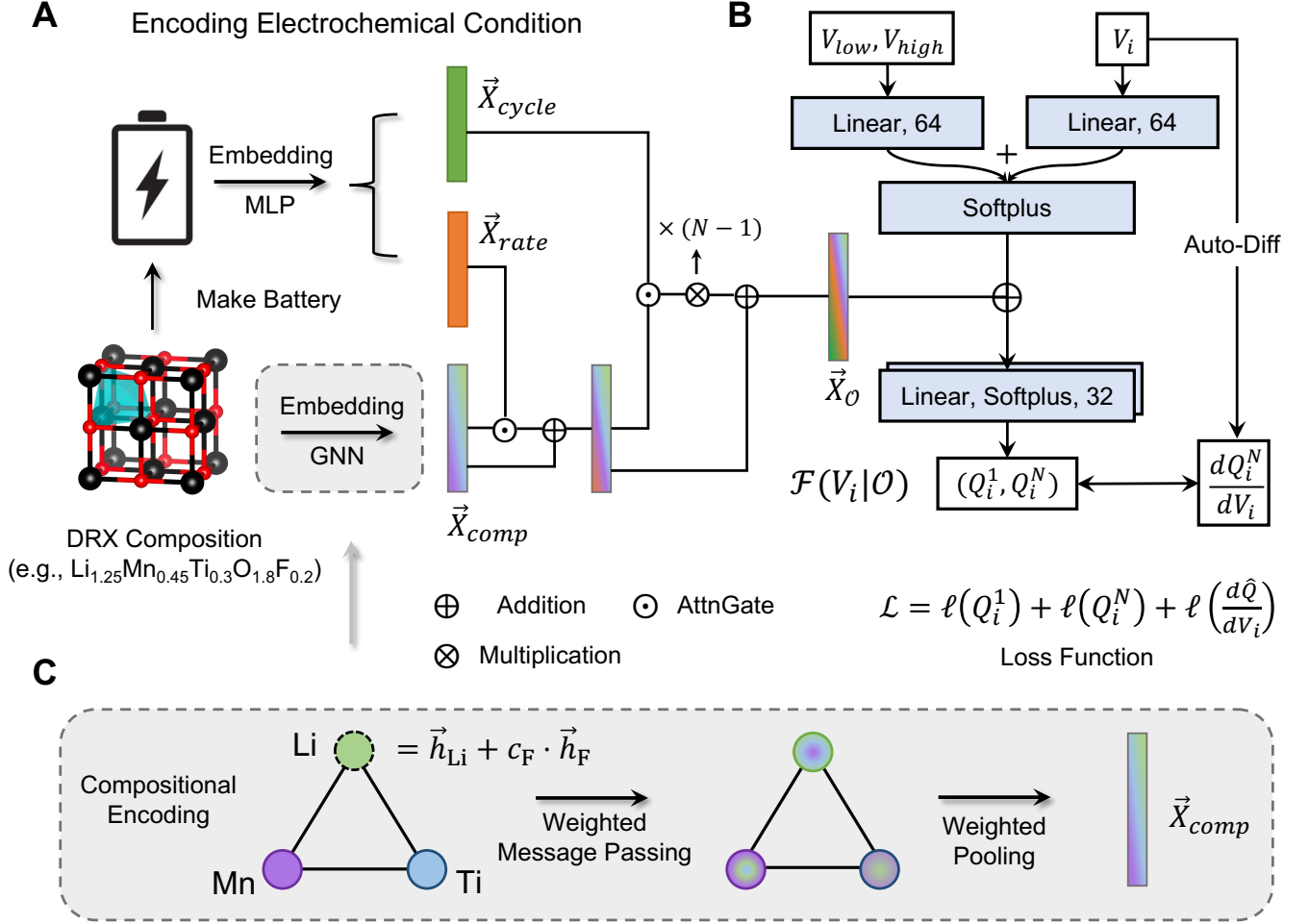


FIG. 2. **Model design of DRXNet:** An end-to-end pipeline that maps $Q_i = \mathcal{F}(V_i|\mathcal{O})$, which consists of the electrochemical condition network \mathcal{O} and the state prediction network \mathcal{F} . (A) The electrochemical condition network encodes the DRX composition, current density rate, and cycle information. The three encoded vectors are synthesized through gated-MLPs with soft-attention to obtain the condition vector \vec{X}_O [20]. (B) The state prediction is approximated as a forward deep neural network that takes the voltage state V_i and cycling voltage window V_{low}, V_{high} as inputs. The encoded condition vector \vec{X}_O is element-wise added in the hidden layer of \mathcal{F} . The circled symbols are all element-wise operations. (C) The message-passing graph neural network (GNN) is used for compositional encoding of DRX, adapted from Roost model [21].

current density rate, and degradation that may have occurred in various cycles. In experiments, the capacity Q is measured by determining the cumulative charge transfer using galvanostatic tests. Another relevant quantity of the voltage profile, dQ/dV , is obtained by taking the derivative of Q with respect to V . The dQ/dV curve is a crucial physical quantity for analyzing characteristic redox potentials from different TMs.

Unlike conventional NMC-based layered cathodes, DRX materials exhibit much more diverse electrochemical performance due to their significantly larger chemical existence and the more complex structure-property relationship involving not only long-range ordering but also short-range ordering [24]. For instance, Mg doping in Mn-based oxyfluoride DRX can increase the discharge capacity while retaining similar voltage-profile shapes [25]; Cr doping in $\text{Li}_{1.2}\text{Mn}_{0.4}\text{Ti}_{0.4}\text{O}_{2.0}$ results in comparable

low-rate capacity but significantly improves the high-rate performance due to the non-topotactic TM migration [26]. These non-linear effects arising from compositional changes make both material design and machine-learning modeling challenging, thereby necessitating a comprehensive, high-fidelity dataset to address such issues.

We have compiled the electrochemical test data related to DRX compounds by mining electronic experimental notebooks in our research over the past five years to construct the DRX Test Dataset (DRX-TD). The dataset contains not only the successful materials using galvanostatic charge/discharge tests in several papers [24–32], but also less well-performing DRX compounds. This endeavor yielded a comprehensive dataset containing 30,000 discharge profiles across 16 different elements (14 metal species) from lab experiments and published literature (see Methods). An individual electrochemical

test is defined as a group of N_{cycle} discharge profiles with a fixed current density rate, where N_{cycle} is the number of cycles conducted in such a test, corresponding to the results obtained from one coin-cell in experiments. The distribution of elements in the DRX-TD is shown in Fig. 1B, where the number in each element’s box represents the number of times that element is presented in a compound for which an electrochemical test is present. The box’s color indicates the number of times that element is presented in a discharge profile. Comprising 19,259 discharge profiles of DRX oxides and 11,604 discharge profiles of oxyfluorides, the dataset offers extensive coverage of major redox-active TMs. Figure 1C displays the histograms of the N_{cycle} and the loading current rates. Most of the electrochemical tests were conducted at a low current rate (20 mA/g).

Building upon the DRX-TD, 100 points were uniformly sampled from the values of V and Q for each discharge profile, resulting in a voltage series $\mathbf{V} = [V_1, V_2, \dots, V_i, \dots]$ and a capacity series $\mathbf{Q} = [Q_1, Q_2, \dots, Q_i, \dots]$. The dQ/dV curve was then calculated based on \mathbf{V} . As dQ/dV is a more intrinsic property for battery materials, including this value in the modeling allows for a more representative analysis of the electrochemical performance of DRX compounds under various conditions (see Methods).

B. DRXNet architecture

DRXNet aims to draw a connection between chemistry and cathode performance by establishing a mapping between \mathbf{V} and \mathbf{Q} for arbitrary cathode compositions under various test conditions. This idea can be conceptualized as identifying a function \mathcal{F} that maps cathode parameters and the voltage state V_i to produce the capacity state Q_i as an output. The function \mathcal{F} is conditionally defined by the parameters \mathcal{O} , which consider the electrode composition, current rate, and cycle number

$$Q_i = \mathcal{F}(V_i | \mathcal{O}). \quad (1)$$

With this intuition, we designed DRXNet with two main components, as shown in Fig. 2A and Fig. 2B: (1) An electrochemical condition network that generates a feature vector $\vec{X}_{\mathcal{O}}$ based on the compound composition and additional features of the electrochemical test information; (2) A state prediction network to approximate the discharge state of the cathode as a function of the voltage state, $Q_i = \mathcal{F}(V_i | \mathcal{O})$, given the electrochemical conditional encoding of \mathcal{O} . For instance, Algorithm 1 demonstrates how DRXNet predicts the first-cycle discharge profile of $\text{Li}_{1.2}\text{Mn}_{0.4}\text{Ti}_{0.4}\text{O}_2$ at a current rate of 20 mA/g between 1.5 and 4.8 V.

Initially, three condition inputs (composition, rate, cycle) are encoded to represent \mathcal{O} . We use **Roost**, a graph neural network model proposed by Goodall and Lee [21], for compositional encoding. **Roost** takes elements as graph nodes and updates the correlation between elements through weighted message passing based on each

Algorithm 1: The workflow of DRXNet with an example of $\text{Li}_{1.2}\text{Mn}_{0.4}\text{Ti}_{0.4}\text{O}_2$

Condition Inputs:

$$\mathcal{O} = \begin{cases} \text{composition} = \text{Li}_{1.2}\text{Mn}_{0.4}\text{Ti}_{0.4}\text{O}_2 \\ \text{rate} = 20 \text{ mA/g}, \\ \text{cycle} = 1 \end{cases}$$

Condition Outputs:

$$\begin{aligned} \vec{X}_{\mathcal{O}_1} &= \vec{X}_{\text{comp}} + \sigma_{f_1}(\vec{X}_{\text{comp}} || \vec{X}_{\text{rate}}) \cdot f_1(\vec{X}_{\text{comp}} || \vec{X}_{\text{rate}}) \\ \vec{X}_{\mathcal{O}_N} &= \vec{X}_{\mathcal{O}_1} + \sigma_{f_2}(\vec{X}_{\mathcal{O}_1} || \vec{X}_{\text{cycle}}) \cdot f_2(\vec{X}_{\mathcal{O}_1} || \vec{X}_{\text{cycle}}) \\ &\quad \cdot \mathbf{W}_n(N-1) \end{aligned}$$

Inputs: $\mathbf{V} = [1.5, \dots, V_i, \dots, 4.8] \rightarrow N$ series

for $i = 1$ **to** N **do**

Compute $Q_i = \mathcal{F}(V_i | \vec{X}_{\mathcal{O}}) \rightarrow \mathcal{F}$ is an NN
end

Outputs: $\mathbf{Q} = [Q_1, \dots, Q_i, \dots, Q_N] \rightarrow N$ series

element’s fractional concentration (Fig. 2C). The nodes are initialized with elemental embedded vectors \vec{h}_s (s : specie) from **mat2vec** to capture as much prior chemical information as possible through text mining of previously published literature [33]. Moreover, we consider only the cation species as independent nodes in **Roost**, treating the anion-species information (fluorine) as a mean-field background, i.e., $\vec{h}'_{\text{Li}} = \vec{h}_{\text{Li}} + c_{\text{F}} \cdot \vec{h}_{\text{F}}$, where c_{F} is the fractional concentration of fluorine and $\vec{h}_{\text{Li/F}}$ is the embedded vector of Li/F. Rate and cycle information is encoded using multi-layer perceptrons (MLPs).

Because the rate and cycle properties are intrinsically affected by the composition, we used gated-MLPs with soft attention for electrochemical condition encoding via a hierarchical network structure [20]. The $\vec{X}_{\mathcal{O}_1} = \vec{X}_{\text{comp}} + \sigma_{f_1}(\vec{X}_{\text{comp}} || \vec{X}_{\text{rate}}) \cdot f_1(\vec{X}_{\text{comp}} || \vec{X}_{\text{rate}})$ is a rate-informed feature vector, where σ_f and f represent MLPs with different activation functions and $||$ denotes the concatenation operation. In addition, the cycle-informed vector $\vec{X}_{\mathcal{O}_N} = \vec{X}_{\mathcal{O}_1} + \sigma_{f_2}(\vec{X}_{\mathcal{O}_1} || \vec{X}_{\text{cycle}}) \cdot f_2(\vec{X}_{\mathcal{O}_1} || \vec{X}_{\text{cycle}}) \cdot \mathbf{W}_n(N-1)$ is linearly dependent on the cycle number with a trainable weight \mathbf{W}_n . As such, the feature vector $\vec{X}_{\mathcal{O}_1}$ is used to represent the 1st cycle and $\vec{X}_{\mathcal{O}_N}$ is used to represent the N -th cycle, respectively.

Lastly, we used several MLPs to construct the state prediction network \mathcal{F} , as shown in Fig. 2B. \mathcal{F} takes the voltage state V_i and working window $V_{\text{low}}, V_{\text{high}}$ as inputs, and the $\vec{X}_{\mathcal{O}}$ is element-wise added to the hidden layer of \mathcal{F} to inform \mathcal{F} of conditions \mathcal{O} (see Methods). As such, the state prediction network \mathcal{F} is constructed as a simple function mapping from the voltage state V_i to the capacity Q_i . In addition, $(dQ/dV)_i$ is obtained by auto-differentiation of \mathcal{F} .

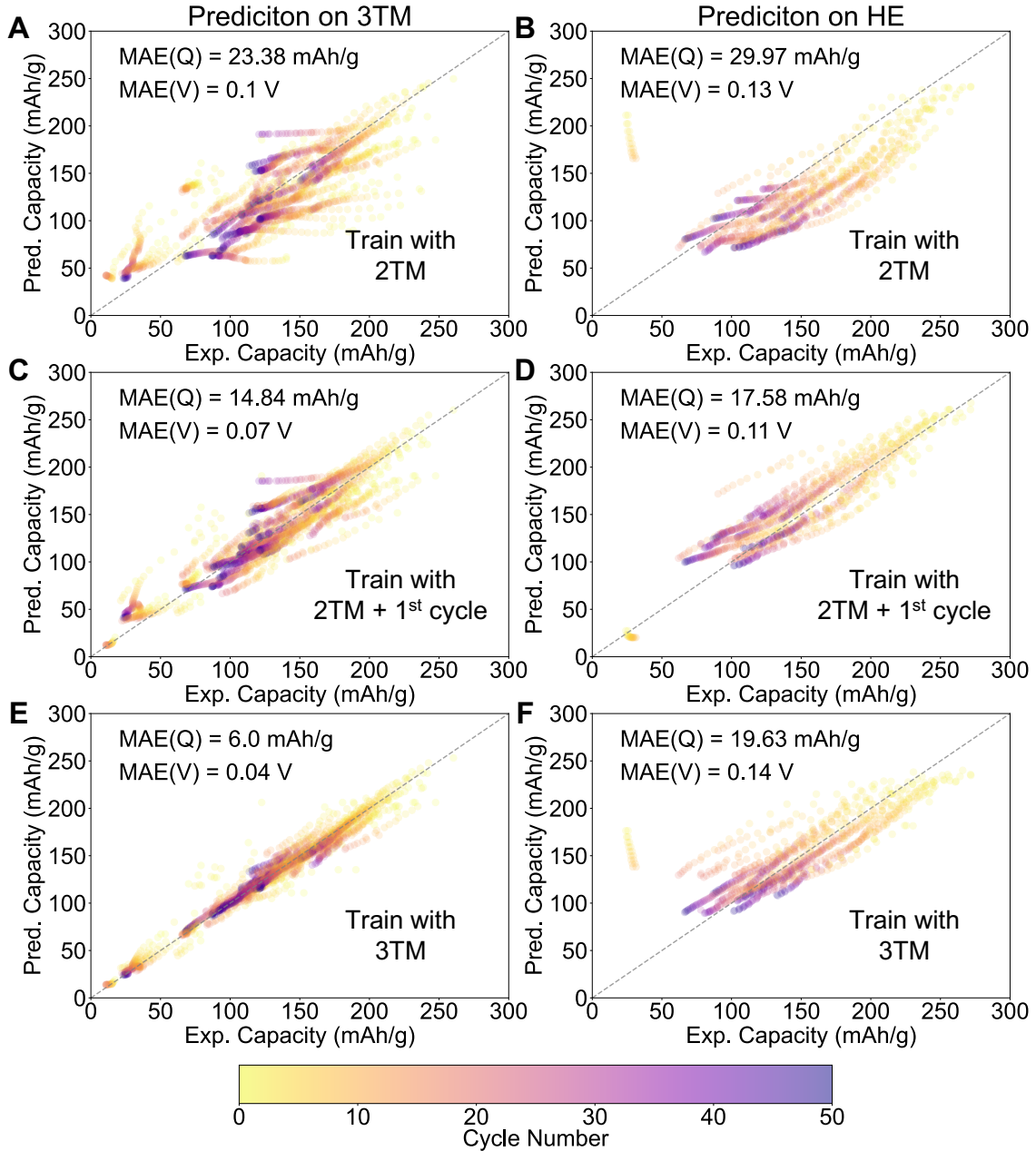


FIG. 3. **Error analysis of DRXNet in compositional space:** (A)–(B) Models are trained on DRX compositions with only two TM species (denoted as 2TM). The models are tested on predicting the delivered capacity between 2.0 and 4.4 V for DRXs composed of three metal species (denoted as 3TM) and higher components (denoted HE for high entropy). (C)–(D) Models are trained on a 2TM dataset along with the first cycles of 3TM and HE as corrected models. The corrected models are tested for subsequent cycles on 3TM and HE to assess the prediction error. (E)–(F) Models are trained on a 3TM dataset and tested on 3TM and HE dataset.

C. Applicability domain

In this section, we explore the scope of DRXNet’s applicability in the realm of composition space. Determination of the applicability domain in battery machine-learning models can be challenging due to the unavailability of a sufficient test dataset, as generating new data necessitates the synthesis of new solid-state materials or

conducting battery cycling tests for weeks to months [13, 34]. For example, simply separating the sequence of voltage and capacity signals $\{V_i, Q_i\}$ into training and test sets can result in data-leakage issues and a failure to represent the expected error in real applications. To evaluate the expressibility and generalization of DRXNet, we designed several experiments by partitioning the dataset based on compositions. The electrochemical tests with

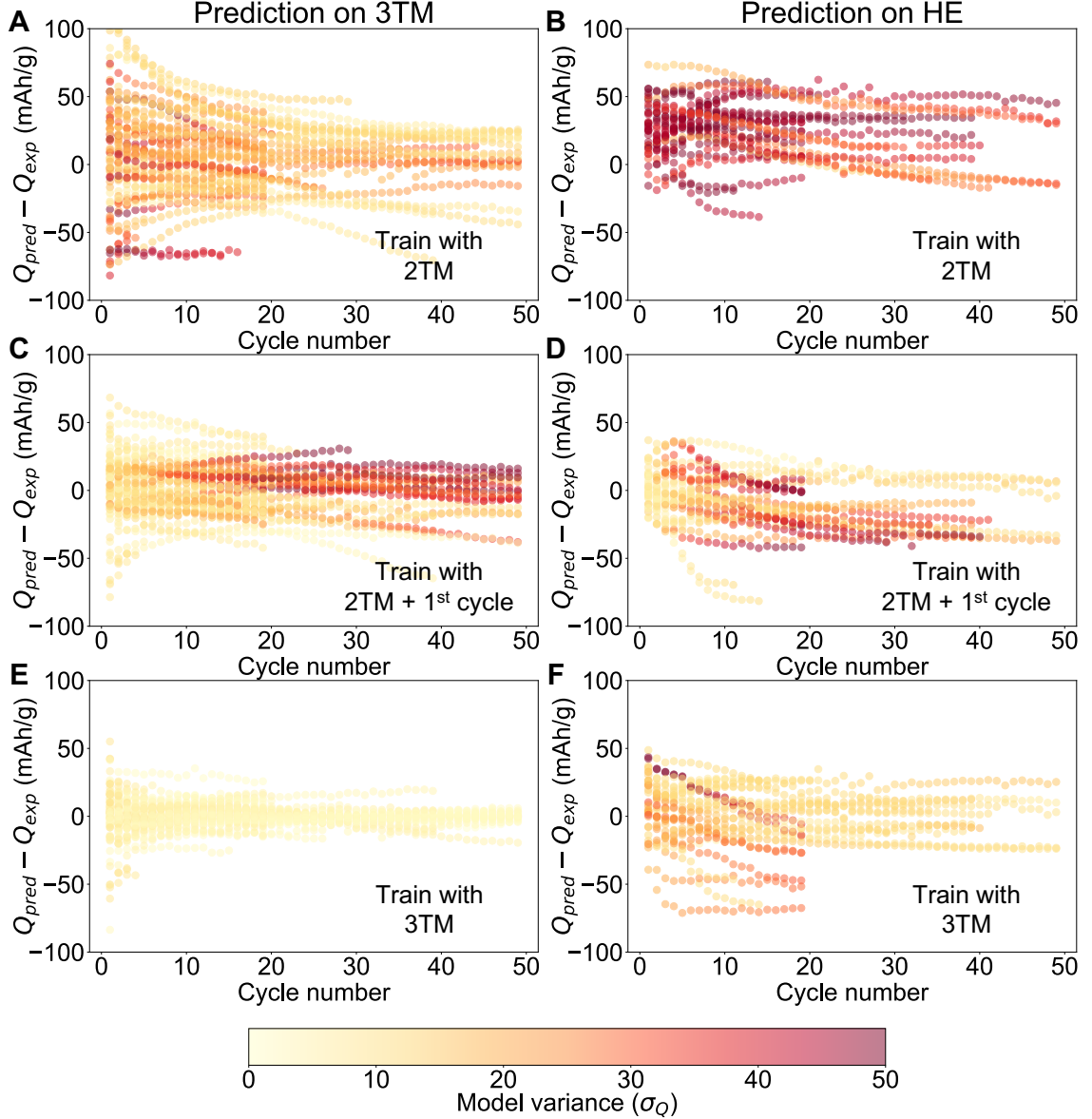


FIG. 4. **Model variance analysis of DRXNet in compositional space:** The prediction error of discharge capacity between 2.0 and 4.4 V (y -axis) *vs.* cycle number (x -axis). The model variance is represented by σ_Q , a standard deviation of the ensemble of the models' prediction, which is plotted as scaled colored dots. (A)–(B): Predictions on 3TM/HE using models trained on the 2TM dataset. (C)–(D): Predictions on 3TM/HE using models trained on both the 2TM dataset and the first cycles of the 3TM/HE dataset. (E)–(F): Predictions on 3TM/HE using models trained on the 3TM dataset.

no more than two metal species (2TM, excluding Li) were designated as the training set, whereas the tests with three metal species (3TM) and higher numbers of TM components (high-entropy, HE) were assigned as test sets. For each test, an ensemble of five independent models was trained to enhance the overall prediction accuracy and robustness and to quantify the model variance. Predictions were generated by averaging the predicted capacities of each DRXNet model.

In Fig. 3A and Fig. 3B, we show the performance of the DRXNet models trained on the 2TM dataset and tested on the 3TM and HE datasets. Mean abso-

lute errors (MAEs) of 0.1/0.13 V for the average voltage ($\bar{V} = \sum_i V_i \Delta Q_i / \sum_i \Delta Q_i$) and 23.38/29.97 mAh/g for the capacity were obtained for the 3TM/HE test datasets, respectively, by comparing the prediction to the experimental Q–V curve within the voltage range of 2.0 – 4.4 V. As a baseline, the mean absolute deviation (MAD) of average voltage is 0.16/0.21 V for 3TM/HE, and the MAD of discharge capacity is 36.59/38.54 mAh/g for 3TM/HE for several comparisons. We found that large prediction errors already occurred at the first cycle and propagated into the subsequent cycles. Notably, a systematic underestimation of capacity is observed for

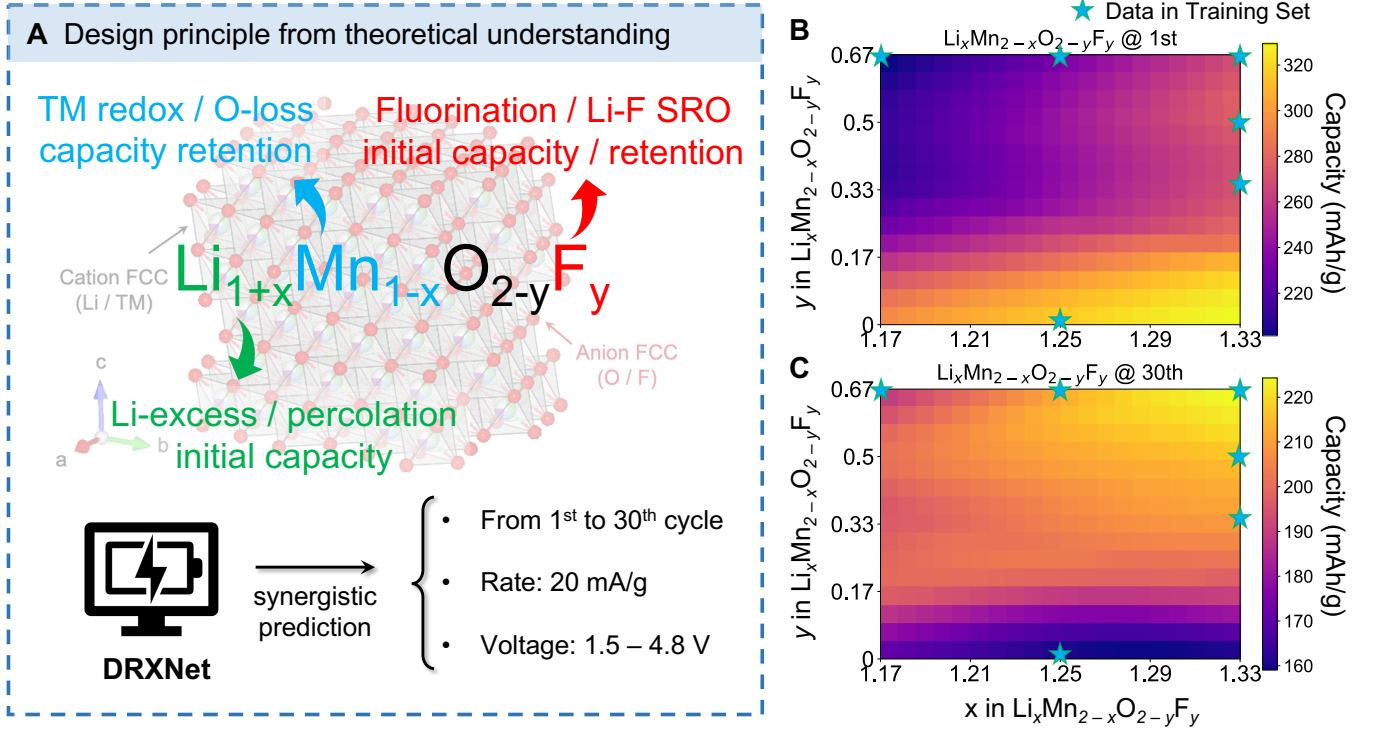


FIG. 5. **Illustration of synergistic predictions of discharge capacity in Li-Mn-O-F DRX systems:** (A) Design principle from theory, where the Li/Mn/F content jointly determines the performance of battery materials (see Ref. [31]). (B) Prediction of discharge capacity for the 1st and 30th cycle in Li-Mn-O-F chemical space between 1.5 – 4.8 V at a current density rate of 20 mA/g, with the blue stars indicating the compositions included in the training set.

HE (Fig. 3B), which can be rationalized by the fact that 2TM represents low-entropy DRX and cannot capture the improved performance arising from the novel high-entropy physics [32].

For practical applications, there are two approaches to improving the model’s accuracy and enhancing its predictive capabilities: (1) new data points can be continuously collected as experiments progress, enabling on-the-fly training with in-situ data to improve predictive performance in data-scarce chemical space; and (2) incorporating a diverse range of information from chemical space and test conditions to deliver well-pretrained models. Regarding (1), we further tested this concept by evaluating the improvement when DRXNet was trained on a dataset containing all 2TM data and was provided with the first cycle data from 3TM/HE materials. The knowledge of just the first cycle data resulted in a reduction of the capacity MAE from 23.38/29.97 mAh/g to 14.84/17.58 mAh/g for 3TM/HE. The enhanced performance achieved by explicitly training with the first cycle indicates that the model can better generalize cycling performance, even when experiments for a specific composition are not extensively sampled. This capability has the potential to significantly reduce the month-long timeframe typically required for electrochemical testing. In regard to (2), we present the results for models trained on the 3TM dataset, where Fig. 3E displays the training

errors (6.0 mAh/g), and the test error on the HE data is 19.63 mAh/g, reduced by 10 mAh/g from those trained on 2TM data.

To rationalize the improvement and assess the expressibility for extrapolation in untrained domains, we examined the prediction error and model variance as a function of cycle number, as shown in Fig. 4. The standard deviation of the prediction from the ensemble of five DRXNet models (σ_Q) was used to represent the model variance as an approximation of how uncertain the predictions are. The 2TM model exhibited moderate model variance for 3TM predictions and high model variance for HE predictions (> 50 mAh/g) as shown in Fig. 4A and B. Training the model with first-cycle data led to a substantial decrease in both the prediction error and model variance for the initial few cycles, although the model variance increased subsequently with the cycle number for untrained domains (Fig. 4C and D).

It is important to note that the models trained on 3TM data show a significantly reduced prediction error and model variance for the HE prediction compared to those obtained when training the 2TM model (Fig. 4F). This finding suggests that the 2TM dataset is not adequate for extracting relevant information and generalizing to other compositions. The scaling to high-component electrodes necessitates capturing more than 2TM correlations or interactions in training the graph neural network. Fail-

ure to do so may lead to systematic prediction errors, as demonstrated in Fig. 3B. When the model is able to acquire sufficient chemical domain knowledge (e.g., 3TM-model), it becomes feasible to extrapolate the electrochemical properties of high-component electrodes.

In the following sections, we will present several examples to illustrate how DRXNet learns the underlying cathode chemistry and assists in the design of new materials. The models used for these applications are pre-trained on all discharge profiles.

D. Synergistic predictions in Li–Mn–O–F

Manganese is an attractive earth-abundant, non-precious TM for next-generation cathode design [27]. Lun *et al.* [31] proposed three primary design degrees of freedom for Mn-based DRX (Fig. 5A): (1) the Li-excess content, which controls the presence of a percolating network creating facile Li diffusion; (2) the Mn content, as low amounts of Mn can lead to severe oxygen redox and poor cyclability; and (3) the fluorine content, which lowers the total cation valence and provides greater freedom to optimize the Li and Mn content. Fluorine modifies cation short-range order through the strong Li–F attraction and lowers the initial capacity [25, 35]. These theoretical principles are highly correlated and exert non-linear effects on performance, making it challenging to predict.

We used DRXNet to predict the discharge capacity between 1.5 and 4.8 V at a current rate of 20 mA/g for the 1st and 30th cycles as a function of Li and F content, which is illustrated in Fig. 5B. The amount and valence of Mn follow directly from the Li and F content. The critical feature of fluorine that has been extensively characterized experimentally is well captured by our model. A higher F content (y in $O_{2-y}F_y$) results in a lower discharge capacity for the 1st cycle but a higher capacity for the 30th cycle. In particular, $Li_{1.333}Mn_{0.667}O_2$ is predicted to have the highest capacity (> 320 mAh/g) for the first cycle but the lowest capacity for the 30th cycle. This prediction is consistent with the understanding the capacity originates from oxygen as the valence of Mn is 4+. Such a large amount of O-redox leads to rapid capacity fade and aligns with the experimental observations of disordered Li_2MnO_3 reported in Ref. [36].

To rationalize the extrapolation ability of DRXNet, we plot the compositions in the training dataset using blue stars in Fig. 5B. It is evident that despite the sparse distribution of training points across the composition map, DRXNet delivers accurate predictions that align with the experimental observations beyond the scope of the training points. As DRXNet is trained on various compositions beyond the Li–Mn–O–F chemical space, the ability to extrapolate to other domains can be attributed to the transfer learning from other F- and non-F-containing compounds. The example in this section demonstrates how practitioners can generalize the design principles

from a data-driven perspective purely starting from experiments.

E. Exploratory search for high-entropy cathodes

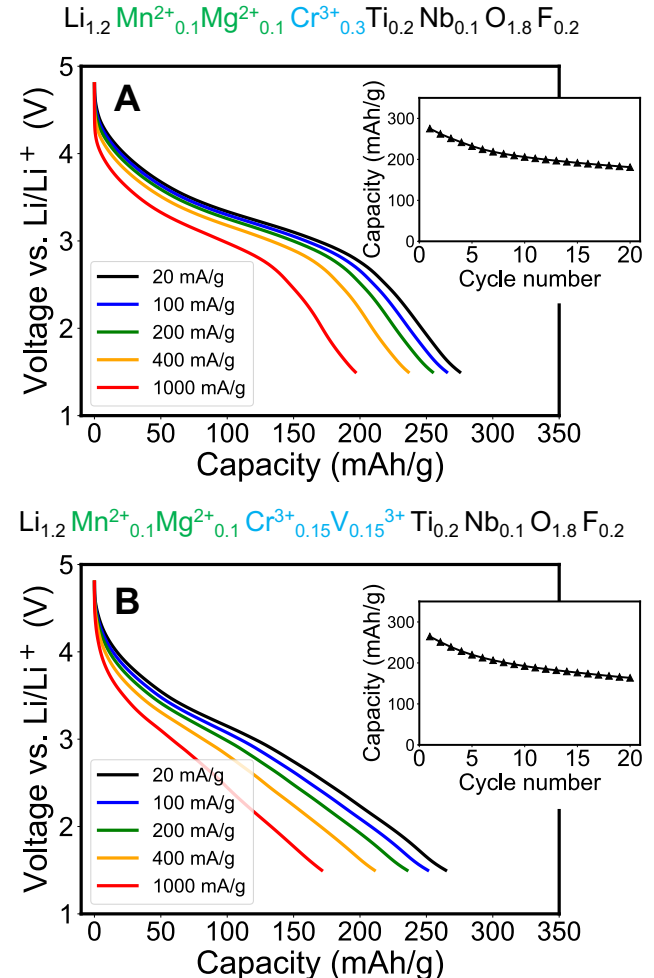


FIG. 6. Predicted discharge profiles of two high-entropy DRX materials with various current density rates (from 20 mA/g to 1000 mA/g). (A) $Li_{1.2}Mn_{0.1}Mg_{0.1}Cr_{0.3}Ti_{0.2}Nb_{0.1}O_{1.8}F_{0.2}$ (HE-1) and (B) $Li_{1.2}Mn_{0.1}Mg_{0.1}Cr_{0.15}V_{0.15}Ti_{0.2}Nb_{0.1}O_{1.8}F_{0.2}$ (HE-2). The inset displays the cycled discharge capacity at a current density rate of 20 mA/g.

High-entropy DRXs are composed of many species and present a vast chemical space to explore for battery materials discovery. In this section, we present two case studies of predicted high-entropy DRXs: $Li_{1.2}Mn_{0.1}Mg_{0.1}Cr_{0.3}Ti_{0.2}Nb_{0.1}O_{1.8}F_{0.2}$ (HE-1) and $Li_{1.2}Mn_{0.1}Mg_{0.1}Cr_{0.15}V_{0.15}Ti_{0.2}Nb_{0.1}O_{1.8}F_{0.2}$ (HE-2). The predicted discharge profiles under various current densities are shown in Fig. 6A and B. A more comprehensive map of other compositions is included in the Supplementary Information.

For HE-1, DRXNet predicts a discharge capacity of 276 mAh/g at a low current rate of 20 mA/g. The discharge voltage profile shows a clear transition from a flat curve to a slopy curve after at around 3 V, which has been widely observed in Mn redox and/or Cr redox-based DRXs [26, 32, 37]. A capacity of 196 mAh/g is predicted at 1000 mA/g, retaining 71% of that delivered at a slow rate of 20 mA/g. From previous studies, multi-elemental substitution (i.e. high-entropy strategy) frustrates unfavorable SRO that leads to sluggish kinetics; Cr incorporation and Cr⁶⁺-migration at high voltage upon delithiation opens up a better-extended 0-TM network for Li transport, both of which can improve the Li diffusion kinetics [26, 32]. DRXNet clearly learns those benefits and extrapolates rationally into electrochemistry prediction of the high-entropy compositions.

As a comparison, partial V³⁺ to Cr³⁺ substitution in HE-1, yielding HE-2 is expected to change the shape of the voltage curves dramatically due to the low potential of V⁵⁺/V³⁺ reduction, which is also predicted using DRXNet as shown in Fig. 6B. It is clearly demonstrated that with V³⁺ incorporation, a nearly constant slope can be observed down to the low-voltage region, which is characteristic for V-based DRX cathodes reported previously [38, 39]. Nevertheless, V⁵⁺ has a similar migration mechanism to enhance Li transport as Cr and is likely to be beneficial for the rate capability [38]. Consistently, although a slightly lower discharge capacity is predicted (266 mAh/g) for HE-2, it retains 171 mAh/g capacity at 1000 mA/g (64% of the capacity at 20 mA/g), which is better than the majority of the DRX cathodes reported to date.

In terms of cyclability, the inset plot shows the predicted discharge capacity of DRX materials within 20 cycles for both materials. A more dramatic capacity drop from the first 5 cycles is predicted, which slows down upon further cycling. This result is in full agreement with experimental findings which indicate that some of the irreversibility in the initial cycles, such as surface carbonate decomposition [40] or cathode-electrolyte interface formation [41]. These examples illustrate how practitioners can effectively use DRXNet to navigate the extensive chemical space of high-entropy DRXs and identify promising candidates for cathode design and optimization.

III. DISCUSSION

The pursuit of carbon neutralization by optimizing the discovery and application of energy-storage materials using AI has long captivated materials scientists. Numerous efforts have been made in this area, and the Battery Data Genome is proposed as a potential breakthrough along with the fast development of AI technologies [9–12]. With this endeavor, we proposed a deep learning approach for battery electrochemistry representation and learning from the experimental data. We

developed a machine-learning model (DRXNet) trained on over 30,000 experimental discharge voltage profiles, encompassing diverse compositional chemistry in DRX cathodes. This was achieved through a novel model design consisting of an electrochemical condition network (\mathcal{O}) and a state prediction network (\mathcal{F}).

The design of the two networks promotes modularity in the architecture, streamlining the optimization and interpretation of each network individually and their learned features. For instance, the hierarchical network structure in \mathcal{O} presents feature vectors for both the first and the N -th cycle (see Eq.(7)). Analyzing the differences between these two vectors can reveal insights into the material’s cyclability fingerprint. Moreover, as highlighted in model training, the loss function is designed for multi-task learning (see Eq.(13)). The 1st and N -th cycle capacities are trained simultaneously in each update. This loss function including two contrastive terms enhances learning efficiency, as each component can focus on specific aspects of the problem (i.e., $\ell(Q^1)$ for composition and rate, $\ell(Q^N)$ for composition, rate, and cycle), leading to improved physical meaning of the network rather than minimizing the average training error.

In addition, the electrochemical condition network design provides flexibility in terms of model application. We recognize that most training datasets are derived from our own experimental results, which do not encompass critical testing parameters such as particle size, electrolyte type, electrode fabrication methods, etc. These factors have been coarsely integrated into the compositional model in our dataset. In principle, researchers can choose to include any factors to design the electrochemical feature vector, depending on the specific problem they are addressing. Given the vast amount and complexity of these properties, a synthetic data collection approach is necessary. Data-mining techniques, such as text mining and figure mining, can automatically retrieve valuable experimental information from decades of published literature [42, 43]. This has the potential to enhance the model’s generalizability and incorporate extensive prior domain knowledge in electrochemical fields.

We would also like to discuss the depth and transferability of DRXNet’s predictive capabilities for exploration, especially for the state prediction network \mathcal{F} . We further tested the electrochemical performance of HE-2 by varying the voltage window and cycling rate, which are the parameters that typically require multiple individual electrochemical tests in experiments. Figure 7A displays the discharge profiles between 2.0 – 4.4 V, with two additional rates tested (10 mA/g for a low rate and 10⁴ mA/g for an extremely high rate). These conditions are infrequently incorporated in our training data. The low rate exhibits a discharge profile very similar to 20 mA/g, which is entirely consistent with experimental findings, as the discharge process at a low rate exhibits a reduced overpotential. The 10 A/g rate discharge profile demonstrates a sharp drop in voltage, reasonably indicating poor performance at an extremely high rate. On

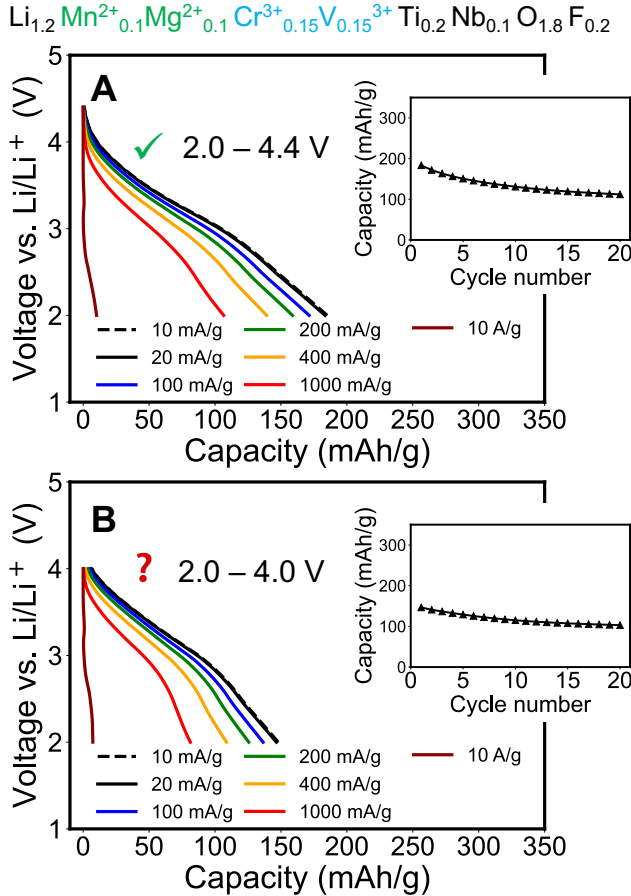


FIG. 7. Predicted discharge profiles with various current density rates (from 10 mA/g to 10 A/g) of $\text{Li}_{1.2}\text{Mn}_{0.1}\text{Mg}_{0.1}\text{Cr}_{0.15}\text{V}_{0.15}\text{Ti}_{0.2}\text{Nb}_{0.1}\text{O}_{1.8}\text{F}_{0.2}$ (HE-2) between (a) 2.0 – 4.4 V and (b) 2.0 – 4.0 V. The inset displays the cycled discharge capacity at a current density rate of 20 mA/g.

the other hand, Figure 7B presents the discharge profiles between 2.0 – 4.0 V, which starts to show some unphysical predictions. Small offsets appear at the beginning of discharge for the low rate profiles, resulting in a non-zero discharge capacity at 4.0 V. We attribute this discrepancy to (1) the connection between voltage state V_i and window $[V_{\text{low}}, V_{\text{high}}]$ being achieved by linear combinations in the hidden layer (Fig. 2B), which is a data-driven encoding and requires training; and (2) a limited number of experiments being conducted with V_{high} lower than 4.0 V, which leads to data scarcity in such voltage range. These two reasons may rationalize why the predictions for 2.0 – 4.4 V show better accuracy (no offsets) while the ones for 2.0 – 4.0 V deviate higher.

Based on the tests, our primary conclusion is that DRXNet exhibits a reasonable ability to learn chemical interactions and generalize to test conditions included in the dataset among different chemical compositions. However, for test conditions that the model has not encountered (e.g., experiments with $V_{\text{high}} < 4.0$ V), discrepan-

cies or unphysical profiles may arise (e.g., non-zero capacity at the beginning). This highlights the data scarcity issue, which arises from human bias and outliers in experimental setups or poorly performing systems, as researchers may discontinue their discovery efforts when faced with unfavorable results [44]. In the future, automated labs can address this scarcity issue by enabling more extensive exploration of the experimental space (e.g., various voltage windows to find the optimal trade-off between energy density and cyclability, along with a combination of different current density rates), even for “failed” experiments [45]. This approach can result in a more comprehensive dataset for building machine-learning models and understanding the electrochemical properties of battery materials.

In conclusion, DRXNet represents a significant step forward in the development of machine-learning models for battery materials research. By continuously refining the model and incorporating additional data and parameters, we anticipate that such a machine-learning framework will play an increasingly critical role in the discovery and optimization of next-generation battery materials.

IV. METHODS

A. Data collection

We collected coin-cell electrochemical test data from our lab starting in 2016 and converted them into a digital format (.json). Each .json file contains information on one individual electrochemical test, including the electrode composition, electrode mass (g), active mass (g), test current rate (mA/g), low and high voltage value of the working window (V), and charge/discharge profiles of N_{cycle} collected cycles.

For the in-house battery tests, the CR2032 coin cells were assembled using commercial 1 M LiPF_6 in an ethylene carbonate and dimethyl carbonate solution (volume ratio 1:1) as the electrolyte, glass microfiber filters (Whatman) as separators, and Li-metal foil (FMC) as the anode. The coin cells were tested on an Arbin battery cycler at room temperature. The cathode consisted of a mixture of active material (DRX), Super C65 carbon black, and polytetrafluoroethylene (PTFE). The capacity signal, collected in units of Ah from the Arbin battery cycler, was normalized to mAh/g using the mass of the active material (active mass). The data from the failed tests (e.g., Arbin cycler breakdown, electrolyte failure, strong signal fluctuations ...) were removed from the dataset (see Supplementary Information for examples).

To enhance the generalization and expressibility of DRXNet, we expanded the dataset by figure mining published voltage profiles in related systems not covered by our lab tests (see Supplementary Information for details), which was accomplished using the `WebPlotDigitizer` [46].

We used the `UnivariateSpline` method to denoise the

experimental profile and compute the dQ/dV curve. One hundred points were uniformly sampled to form the voltage series $\mathbf{V} = [V_0, V_1, \dots, V_i, \dots]$ for each discharge profile, and the capacity series and dQ/dV series were calculated accordingly from \mathbf{V} .

B. Model design

1. Preliminaries

We define a linear layer with trainable weight \mathbf{W} and bias \mathbf{b} as

$$L(\vec{X}) = \vec{X}\mathbf{W} + \mathbf{b}. \quad (2)$$

A multi-layer perceptron (MLP) is denoted as

$$\phi(\vec{X}) = \sigma \left(L(\vec{X}) \right) = \sigma \circ L(\vec{X}), \quad (3)$$

where σ is a non-linear activation function.

2. Compositional encoding

For elemental information, each element is first embedded into a 200-dimensional vector using `mat2vec` [33]. `Roost` (Representation Learning from Stoichiometry) model is used for compositional encoding [21], which is a graph neural network (GNN) with message passings as follows:

$$\begin{aligned} \vec{h}_i^{t+1} &= \vec{h}_i^t + \sum_{j,m} a_{i,j}^{t,m} \cdot \sigma_g \circ L_c \left(\vec{h}_i^t || \vec{h}_j^t \right), \\ a_{i,j}^{t,m} &= \frac{w_j \exp(e_{i,j}^{t,m})}{\sum_k w_k \exp(e_{i,k}^{t,m})}, \quad e_{i,k}^{t,m} = \sigma_g \circ L_a \left(\vec{h}_i^t || \vec{h}_k^t \right). \end{aligned} \quad (4)$$

In these equations, \vec{h}_i^t represents the t -th hidden layer for the i -th element; $||$ denotes the concatenation operation; and the soft-attention coefficient $a_{i,j}^{t,m}$ describes the interaction between elements i and j , with m as the index of multi-head attention. L_c and L_a denote the linear layer for the core and attention layer, respectively. The fractional concentration w_j of element j depends on the specific compound (e.g., $w_j = 0.6/0.2/0.2$ for Li/Mn/Ti in $\text{Li}_{1.2}\text{Mn}_{0.4}\text{Ti}_{0.4}\text{O}_{2.0}$). σ_g is the SiLu activation function. After n graph convolution layers, the encoded composition vector \vec{X}_{comp} is obtained by average pooling over the elements with weighted attention

$$\vec{X}_{\text{comp}} = \text{Pooling} \left[\frac{w_i \exp \left(\sigma_g \circ L_a(\vec{h}_i^n) \right)}{\sum_k \exp \left(\sigma_g \circ L_a(\vec{h}_k^n) \right)} \cdot \left(\sigma_g \circ L_c(\vec{h}_i^n) \right) \right] \quad (5)$$

3. Electrochemical condition encoding

The electrochemical test primarily involves two pieces of information: the current density rate and cycle number. We use MLPs to encode the rate and cycle number:

$$\vec{X}_{\text{rate}} = \sigma_g \circ L(\text{rate}), \quad \vec{X}_{\text{cycle}} = \sigma_g \circ L(\text{cycle}). \quad (6)$$

As the actual rate and cycle performance are strongly correlated with cathode materials, the relationship between the composition, rate, and cycle is synthesized using gated-MLPs with soft attention[20]:

$$\begin{aligned} \vec{X}_{\mathcal{O}_1} &= \vec{X}_{\text{comp}} + \sigma_{f_1}(\vec{X}_{\text{comp}} || \vec{X}_{\text{rate}}) \cdot f_1(\vec{X}_{\text{comp}} || \vec{X}_{\text{rate}}) \\ \vec{X}_{\mathcal{O}_N} &= \vec{X}_{\mathcal{O}_1} + \sigma_{f_2}(\vec{X}_{\mathcal{O}_1} || \vec{X}_{\text{cycle}}) \cdot f_2(\vec{X}_{\mathcal{O}_1} || \vec{X}_{\text{cycle}}) \cdot \mathbf{W}_n(N-1) \end{aligned} \quad (7)$$

where $\sigma_f = \sigma_s \circ B \circ L$ is an MLP, σ_s is the Sigmoid activation function, and $f = \sigma_g \circ B \circ L$ is an MLP with SiLu activation function σ_g . The BatchNormalization layer B is added before the activation function. In this equation, $\vec{X}_{\mathcal{O}_1}$ is a feature vector jointly determined by the composition and rate information, which is used to predict the first cycle property. $\vec{X}_{\mathcal{O}_N}$ is a feature vector jointly determined by the composition, rate, and cycle information, which is used to predict the N -th cycle property. The difference between $\vec{X}_{\mathcal{O}_1}$ and $\vec{X}_{\mathcal{O}_N}$ is linearly dependent on the number of cycles with a trainable weight \mathbf{W}_n , allowing the model to learn cycle performance contrastively.

4. State prediction network

The state prediction network (\mathcal{F}) takes the inputs of voltage state (V_i) and outputs the discharge-capacity state (Q_i)

$$Q_i = \mathcal{F}(V_i | \mathcal{O}). \quad (8)$$

In practice, the voltage profile is measured within the applied voltage window $[V_{\text{low}}, V_{\text{high}}]$. To accommodate the voltage window in the discharge state prediction, the first layer in \mathcal{F} is encoded via an MLP:

$$\vec{Z}_i^0 = \sigma_{\mathcal{F}} \left([V_{\text{low}}, V_{\text{high}}]^T \mathbf{W}_1 + [V_i]^T \mathbf{W}_2 \right), \quad (9)$$

where $\sigma_{\mathcal{F}}(\cdot)$ is the Softplus activation function and $\mathbf{W}_{1/2}$ is the trainable weight. We used a ResNet-like structure to incorporate the test-condition information from $\vec{X}_{\mathcal{O}}$ [47]

$$\begin{aligned} \vec{Z}_i^1 &= \sigma_{\mathcal{F}} \circ L_0 \left(\vec{Z}_i^0 + \vec{X}_{\mathcal{O}_1} \right) \\ \vec{Z}_i^N &= \sigma_{\mathcal{F}} \circ L_0 \left(\vec{Z}_i^0 + \vec{X}_{\mathcal{O}_N} \right) \end{aligned} \quad (10)$$

The state of capacity is obtained by

$$\begin{aligned} Q_i^1 &= \sigma_{\mathcal{F}} \circ L_2 \circ \sigma_{\mathcal{F}} \circ L_1(\vec{Z}_i^1) \\ Q_i^N &= \sigma_{\mathcal{F}} \circ L_2 \circ \sigma_{\mathcal{F}} \circ L_1(\vec{Z}_i^N) \end{aligned} \quad (11)$$

where Q_i^1 is the capacity for the first cycle and Q_i^N is the capacity for the N -th cycle. Because the discharge capacity is always positive, $\sigma_{\mathcal{F}}$ is added to constrain the predicted capacity to be positive and accelerate the training process. dQ/dV for the redox potential can be obtained via PyTorch auto-differentiation [48]

$$\left. \frac{dQ}{dV} \right|_i = \text{AutoDiff}(Q_i, V_i). \quad (12)$$

C. Model training

The model is trained to minimize the sum of multi-task losses for the capacity of the first cycle, the n -th cycle, and dQ/dV :

$$\mathcal{L} = w_Q \ell(Q_i^N) + w_{dQ} \ell\left(\frac{dQ}{dV_i}\right) + w_{Q_1} \ell(Q_i^1) + \mathcal{R}. \quad (13)$$

The MSE loss function is used for $\ell(Q_i^N)$ and $\ell(\frac{dQ}{dV_i})$, whereas the MAE loss function is employed for the first cycle as a contrastive term $\ell(Q_i^1)$. The weights for Q_i^N , dQ/dV , and Q_i^1 are set to $w_Q = 1$, $w_{dQ} = 1$, and $w_{Q_1} = 5$. The term \mathcal{R} represents regularization, which consists of two parts: (1) an ℓ_2 -norm regularization of the network's parameters $\|\theta\|_2$ and (2) a smoothing term $\|dQ/dc\|_2$ to avoid large, unphysical performance fluctuations (c denotes the fractional concentration of elements). The weight of regularization is 10^{-4} .

To make predictions, an ensemble of five independent models was trained to make predictions. Each model was trained with a batch size of 1024 within 30 epochs. The Adam optimizer was used with 10^{-3} as the initial learning rate. The ExponentialLR scheduler was used to adjust the learning rate with a decay of 0.9 per epoch.

V. ACKNOWLEDGMENTS

This work was primarily supported by the U.S. Department of Energy, Office of Science, Office of Basic Energy Sciences, Materials Sciences and Engineering Division under Contract No. DE-AC0205CH11231 (Materials Project program KC23MP). The data collection in this work was supported by the Assistant Secretary for Energy Efficiency and Renewable Energy, Vehicle Technologies Office, under the Advanced Battery Materials Research (BMR) Program, of the US Department of Energy (DOE) under contract No. DE-AC0205CH11231. The computational modeling in this work was supported by the computational resources provided by the Extreme Science and Engineering Discovery Environment (XSEDE), supported by National Science Foundation grant number ACI1053575; the National Energy Research Scientific Computing Center (NERSC); and the Lawrence computational cluster resource provided by the IT Division at the Lawrence Berkeley National Laboratory. The authors thank Huiwen Ji, Jianping Huang, and Zijian Cai for their help in experimental data collection and Yifan Chen for valuable discussions.

VI. AVAILABILITY

The models will be released after review or upon reasonable request.

VII. COMPETING INTERESTS

The authors declare no competing interests.

-
- [1] E. A. Olivetti, G. Ceder, G. G. Gaustad, and X. Fu, Lithium-Ion Battery Supply Chain Considerations: Analysis of Potential Bottlenecks in Critical Metals, *Joule* **1**, 229 (2017).
 - [2] L. Xie, C. Singh, S. K. Mitter, M. A. Dahleh, and S. S. Oren, Toward carbon-neutral electricity and mobility: Is the grid infrastructure ready?, *Joule* **5**, 1908 (2021).
 - [3] Y. Tian, G. Zeng, A. Rutt, T. Shi, H. Kim, J. Wang, J. Koettgen, Y. Sun, B. Ouyang, T. Chen, Z. Lun, Z. Rong, K. Persson, and G. Ceder, Promises and Challenges of Next-Generation "Beyond Li-ion" Batteries for Electric Vehicles and Grid Decarbonization, *Chemical Reviews* **121**, 1623 (2021).
 - [4] J. B. Goodenough and Y. Kim, Challenges for rechargeable Li batteries, *Chemistry of Materials* **22**, 587 (2010).
 - [5] C. Lv, X. Zhou, L. Zhong, C. Yan, M. Srinivasan, Z. W. Seh, C. Liu, H. Pan, S. Li, Y. Wen, and Q. Yan, Machine Learning: An Advanced Platform for Materials Development and State Prediction in Lithium-Ion Batteries, *Advanced Materials* **34**, 2101474 (2022).
 - [6] Z. Ahmad, T. Xie, C. Maheshwari, J. C. Grossman, and V. Viswanathan, Machine Learning Enabled Computational Screening of Inorganic Solid Electrolytes for Suppression of Dendrite Formation in Lithium Metal Anodes, *ACS Central Science* **4**, 996 (2018).
 - [7] B. Deng, P. Zhong, K. Jun, K. Han, C. J. Bartel, and G. Ceder, CHGNet: Pretrained universal neural network potential for charge-informed atomistic modeling, *arXiv preprint arXiv:2302.14231* (2023).
 - [8] K. A. Severson, P. M. Attia, N. Jin, N. Perkins, B. Jiang, Z. Yang, M. H. Chen, M. Aykol, P. K. Herring, D. Fraggadakis, M. Z. Bazant, S. J. Harris, W. C. Chueh, and R. D. Braatz, Data-driven prediction of battery cycle life before capacity degradation, *Nature Energy* **4**, 383 (2019).
 - [9] P. K. Jones, U. Stimming, and A. A. Lee, Impedance-based forecasting of lithium-ion battery performance amid uneven usage, *Nature Communications* **13**, 1 (2022).

- [10] M. Aykol, C. B. Gopal, A. Anapolsky, P. K. Herring, B. van Vlijmen, M. D. Berliner, M. Z. Bazant, R. D. Braatz, W. C. Chueh, and B. D. Storey, Perspective—Combining Physics and Machine Learning to Predict Battery Lifetime, *Journal of The Electrochemical Society* **168**, 030525 (2021).
- [11] P. M. Attia, A. Grover, N. Jin, K. A. Severson, T. M. Markov, Y.-H. Liao, M. H. Chen, B. Cheong, N. Perkins, Z. Yang, P. K. Herring, M. Aykol, S. J. Harris, R. D. Braatz, S. Ermon, and W. C. Chueh, Closed-loop optimization of fast-charging protocols for batteries with machine learning, *Nature* **578**, 397 (2020).
- [12] L. Ward, S. Babinec, E. J. Dufek, D. A. Howey, V. Viswanathan, M. Aykol, D. A. Beck, B. Blaiszik, B.-R. Chen, G. Crabtree, S. Clark, V. De Angelis, P. Dechent, M. Dubarry, E. E. Eggleton, D. P. Finegan, I. Foster, C. B. Gopal, P. K. Herring, V. W. Hu, N. H. Paulson, Y. Preger, D. Uwe-Sauer, K. Smith, S. W. Snyder, S. Sripad, T. R. Tanim, and L. Teo, Principles of the Battery Data Genome, *Joule* **6**, 2253 (2022).
- [13] A. D. Sendek, B. Ransom, E. D. Cubuk, L. A. Pellauchoud, J. Nanda, and E. J. Reed, Machine Learning Modeling for Accelerated Battery Materials Design in the Small Data Regime, *Advanced Energy Materials* **12**, 2200553 (2022).
- [14] R. J. Clément, Z. Lun, and G. Ceder, Cation-disordered rocksalt transition metal oxides and oxyfluorides for high energy lithium-ion cathodes, *Energy & Environmental Science* **13**, 345 (2020).
- [15] B. Key, M. Morcrette, J.-M. Tarascon, and C. P. Grey, Pair Distribution Function Analysis and Solid State NMR Studies of Silicon Electrodes for Lithium Ion Batteries: Understanding the (De)lithiation Mechanisms, *Journal of the American Chemical Society* **133**, 503 (2011).
- [16] L. Li, Z. Lun, D. Chen, Y. Yue, W. Tong, G. Chen, G. Ceder, and C. Wang, Fluorination-Enhanced Surface Stability of Cation-Disordered Rocksalt Cathodes for Li-Ion Batteries, *Advanced Functional Materials* **31**, 2101888 (2021).
- [17] R. J. Clément, D. Kitchaev, J. Lee, and Gerbrand Ceder, Short-Range Order and Unusual Modes of Nickel Redox in a Fluorine-Substituted Disordered Rocksalt Oxide Lithium-Ion Cathode, *Chemistry of Materials* **30**, 6945 (2018).
- [18] P. Zhong, T. Chen, L. Barroso-Luque, F. Xie, and G. Ceder, An $\ell_0\ell_2$ -norm regularized regression model for construction of robust cluster expansions in multicomponent systems, *Physical Review B* **106**, 024203 (2022).
- [19] L. Barroso-Luque, P. Zhong, J. H. Yang, F. Xie, T. Chen, B. Ouyang, and G. Ceder, Cluster expansions of multicomponent ionic materials: Formalism and methodology, *Physical Review B* **106**, 144202 (2022).
- [20] T. Xie and J. C. Grossman, Crystal Graph Convolutional Neural Networks for an Accurate and Interpretable Prediction of Material Properties, *Physical Review Letters* **120**, 145301 (2018).
- [21] R. E. A. Goodall and A. A. Lee, Predicting materials properties without crystal structure: deep representation learning from stoichiometry, *Nature Communications* **11**, 6280 (2020).
- [22] A. Urban, A. Abdellahi, S. Dacek, N. Artrith, and G. Ceder, Electronic-Structure Origin of Cation Disorder in Transition-Metal Oxides, *Physical Review Letters* **119**, 1 (2017).
- [23] J. Lee, J. K. Papp, R. J. Clément, S. Sallis, D.-H. Kwon, T. Shi, W. Yang, B. D. McCloskey, and G. Ceder, Mitigating oxygen loss to improve the cycling performance of high capacity cation-disordered cathode materials, *Nature Communications* **8**, 981 (2017).
- [24] H. Ji, A. Urban, D. A. Kitchaev, D.-H. Kwon, N. Artrith, C. Ophus, W. Huang, Z. Cai, T. Shi, J. C. Kim, H. Kim, and G. Ceder, Hidden structural and chemical order controls lithium transport in cation-disordered oxides for rechargeable batteries, *Nature Communications* **10**, 592 (2019).
- [25] P. Zhong, Z. Cai, Y. Zhang, R. Giovine, B. Ouyang, G. Zeng, Y. Chen, R. Clément, Z. Lun, and G. Ceder, Increasing Capacity in Disordered Rocksalt Cathodes by Mg Doping, *Chemistry of Materials* **32**, 10728 (2020).
- [26] J. Huang, P. Zhong, Y. Ha, D.-h. Kwon, M. J. Crafton, Y. Tian, M. Balasubramanian, B. D. McCloskey, W. Yang, and G. Ceder, Non-topotactic reactions enable high rate capability in Li-rich cathode materials, *Nature Energy* **6**, 706 (2021).
- [27] J. Lee, D. A. Kitchaev, D.-h. Kwon, C.-w. Lee, J. K. Papp, Y.-s. Liu, Z. Lun, R. J. Clément, T. Shi, B. D. McCloskey, J. Guo, M. Balasubramanian, and G. Ceder, Reversible $\text{Mn}^{2+}/\text{Mn}^{4+}$ double redox in lithium-excess cathode materials, *Nature* **556**, 185 (2018).
- [28] D. A. Kitchaev, Z. Lun, W. D. Richards, H. Ji, R. J. Clément, M. Balasubramanian, D.-H. Kwon, K. Dai, J. K. Papp, T. Lei, B. D. McCloskey, W. Yang, J. Lee, and G. Ceder, Design principles for high transition metal capacity in disordered rocksalt Li-ion cathodes, *Energy & Environmental Science* **11**, 2159 (2018).
- [29] Z. Lun, B. Ouyang, D. A. Kitchaev, R. J. Clément, J. K. Papp, M. Balasubramanian, Y. Tian, T. Lei, T. Shi, B. D. McCloskey, J. Lee, and G. Ceder, Improved Cycling Performance of Li-Excess Cation-Disordered Cathode Materials upon Fluorine Substitution, *Advanced Energy Materials* **9**, 1802959 (2019).
- [30] H. Ji, D. A. Kitchaev, Z. Lun, H. Kim, E. Foley, D.-H. Kwon, Y. Tian, M. Balasubramanian, M. Bianchini, C. Cai, R. J. Clément, J. C. Kim, and G. Ceder, Computational Investigation and Experimental Realization of Disordered High-Capacity Li-Ion Cathodes Based on Ni Redox, *Chemistry of Materials* **31**, 2431 (2019).
- [31] Z. Lun, B. Ouyang, Z. Cai, R. J. Clément, D.-H. Kwon, J. Huang, J. K. Papp, M. Balasubramanian, Y. Tian, B. D. McCloskey, H. Ji, H. Kim, D. A. Kitchaev, and G. Ceder, Design Principles for High-Capacity Mn-Based Cation-Disordered Rocksalt Cathodes, *Chem* **6**, 153 (2020).
- [32] Z. Lun, B. Ouyang, D.-h. Kwon, Y. Ha, E. E. Foley, T.-Y. Huang, Z. Cai, H. Kim, M. Balasubramanian, Y. Sun, J. Huang, Y. Tian, H. Kim, B. D. McCloskey, W. Yang, R. J. Clément, H. Ji, and G. Ceder, Cation-disordered rocksalt-type high-entropy cathodes for Li-ion batteries, *Nature Materials* **20**, 214 (2021).
- [33] V. Tshitoyan, J. Dagdelen, L. Weston, A. Dunn, Z. Rong, O. Kononova, K. A. Persson, G. Ceder, and A. Jain, Unsupervised word embeddings capture latent knowledge from materials science literature, *Nature* **571**, 95 (2019).
- [34] C. Sutton, M. Boley, L. M. Ghiringhelli, M. Rupp, J. Vreeken, and M. Scheffler, Identifying domains of applicability of machine learning models for materials science, *Nature Communications* **11**, 4428 (2020).

- [35] B. Ouyang, N. Artrith, Z. Lun, Z. Jadidi, D. A. Kitchaev, H. Ji, A. Urban, and G. Ceder, Effect of Fluorination on Lithium Transport and Short-Range Order in Disordered-Rocksalt-Type Lithium-Ion Battery Cathodes, *Advanced Energy Materials* **10**, 1903240 (2020).
- [36] R. Kataoka, T. Kojima, and N. Takeichi, Electrochemical Property of Li-Mn Cation Disordered Li-Rich Li₂MnO₃ with NaCl Type Structure, *Journal of The Electrochemical Society* **165**, A291 (2018).
- [37] S. Ren, R. Chen, E. Maawad, O. Dolotko, A. A. Guda, V. Shapovalov, D. Wang, H. Hahn, and M. Fichtner, Improved Voltage and Cycling for Li⁺ Intercalation in High-Capacity Disordered Oxyfluoride Cathodes, *Advanced Science* **2**, 1500128 (2015).
- [38] M. Nakajima and N. Yabuuchi, Lithium-Excess Cation-Disordered Rocksalt-Type Oxide with Nanoscale Phase Segregation: Li_{1.25}Nb_{0.25}V_{0.5}O₂, *Chemistry of Materials* **29**, 6927 (2017).
- [39] R. Chen, S. Ren, M. Yavuz, A. A. Guda, V. Shapovalov, R. Witter, M. Fichtner, and H. Hahn, Li⁺ intercalation in isostructural Li₂VO₃ and Li₂VO₂F with O²⁻ and mixed O²⁻/F⁻ anions, *Physical Chemistry Chemical Physics* **17**, 17288 (2015).
- [40] L. A. Kaufman and B. D. McCloskey, Surface Lithium Carbonate Influences Electrolyte Degradation via Reactive Oxygen Attack in Lithium-Excess Cathode Materials, *Chemistry of Materials* **33**, 4170 (2021).
- [41] K. Edström, T. Gustafsson, and J. Thomas, The cathode-electrolyte interface in the Li-ion battery, *Electrochimica Acta* **50**, 397 (2004).
- [42] O. Kononova, T. He, H. Huo, A. Trewartha, E. A. Olivetti, and G. Ceder, Opportunities and challenges of text mining in materials research, *iScience* **24**, 102155 (2021).
- [43] V. Baibakova, M. Elzouka, S. Lubner, R. Prasher, and A. Jain, Optical emissivity dataset of multi-material heterogeneous designs generated with automated figure extraction, *Scientific Data* **9**, 589 (2022).
- [44] P. Raccuglia, K. C. Elbert, P. D. F. Adler, C. Falk, M. B. Wenny, A. Mollo, M. Zeller, S. A. Friedler, J. Schrier, and A. J. Norquist, Machine-learning-assisted materials discovery using failed experiments, *Nature* **533**, 73 (2016).
- [45] N. J. Szymanski, Y. Zeng, H. Huo, C. J. Bartel, H. Kim, and G. Ceder, Toward autonomous design and synthesis of novel inorganic materials, *Materials Horizons* **8**, 2169 (2021).
- [46] A. Rohatgi, Webplotdigitizer: Version 4.6 (2022).
- [47] K. He, X. Zhang, S. Ren, and J. Sun, Deep Residual Learning for Image Recognition, in *2016 IEEE Conference on Computer Vision and Pattern Recognition (CVPR)*, Vol. 2016-Decem (IEEE, 2016) pp. 770–778.
- [48] A. Paszke, S. Gross, F. Massa, A. Lerer, J. Bradbury, G. Chanan, T. Killeen, Z. Lin, N. Gimelshein, L. Antiga, *et al.*, Pytorch: An imperative style, high-performance deep learning library, *Advances in neural information processing systems* **32** (2019).